Upside-Down Molding Approach for Geometrical Parameter-Tunable Photonic Perovskite Nanostructures

Lebin Nie, Wai Kit Ng, ZhiFu Liang, Xingang Ren, Tingbin Yang, Guanding Mei, Chi Wah Leung, Kam Sing Wong*, and Wallace C.H. Choy*

Lebin Nie − Department of Electrical and Electronic Engineering, The University of Hong Kong, Hong Kong, Special Administrative Region 999077, China

Wai Kit Ng − Department of Physics and and William Mong Institute of Nano Science and Technology, The Hong Kong University of Science and Technology, Hong Kong, Special Administrative Region 999077, China

ZhiFu Liang − Department of Electrical and Electronic Engineering, The University of Hong Kong, Hong Kong, Special Administrative Region 999077, China

Xingang Ren − Key Laboratory of Intelligent Computing & Signal Processing, Anhui University, Hefei 230036, China

Tingbin Yang − Core Research Facilities, Southern University of Science and Technology, Shenzhen 518055, China

Guanding Mei − Department of Electrical and Electronic Engineering, The University of Hong Kong, Hong Kong, Special Administrative Region 999077, China

Chi Wah Leung − Department of Applied Physics, The Hong Kong Polytechnic University, Kowloon, Hong Kong Special Administrative Region 999077, China;

Corresponding Authors

Kam Sing Wong − Department of Physics and and William Mong Institute of Nano Science and Technology, The Hong Kong University of Science and Technology, Hong Kong, Special Administrative Region 999077, China; Email: phkswong@ust.hk

Wallace C.H. Choy − Department of Electrical and Electronic Engineering, The University of Hong Kong, Hong Kong, Special Administrative Region 999077, China; Email: chchoy@eee.hku.hk

Abstract

Considering that the periodic photonic nanostructures are commonly realized by expensive nanofabrication processes and the tunability of structure parameters is limited and complicated, we demonstrate a solution-processed upside-down molding method to fabricate photonic resonators on perovskites with a pattern geometry controllable to a certain extent. This upside-down approach not only reveals the effect of capillary force during the imprinting but also can control the waveguide layer thickness due to the inversion of the perovskite membranes.

Introduction

The precisely designed photonic crystal structure has been proved to improve the optical properties of semiconductors such as III–V compound semiconductors for device applications, including enhancing light absorption in solar cells (1,2) and photodetectors, (3) improving light emission in light-emitting diodes (LEDs), (4,5) and providing feedback in distributed feedback (DFB) laser devices. (6−8) However, conventional nonsolution nanoimprint lithography (NIL) including hot embossing, thermoplastic, or UV-based nanoimprint involves time-consuming and cumbersome processes under extreme conditions such as high temperature and pressure. (9) For instance, in typical thermoplastic NIL, the imprint resist polymer should be heated above the glass transition temperature (up to 200 °C) and the pattern is pressed into the soft polymer under a pressure of 13 MPa. (10) Therefore, it is highly desirable to realize the high-performance optical nanoresonators by a simple room-temperature solution process and to address the ever-demanding low-cost and efficient optoelectronic devices.

The lead halide perovskite has attracted extensive attention from worldwide researchers owing to its advantages of high quantum efficiency, (11) band gap tunability, (12) large absorption coefficient, (13,14) and solution processability. (15,16) Compared with fast progress on the planar perovskite thin film in optoelectronic devices, (17−19) the periodically structured perovskites are less reported because of the complicated fabrication procedures and poor controllability. It is a potential alternative to boost the performance of devices by endowing the planar perovskite film with a specific photonic nanostructure. One method is directly imprinting patterns on solid perovskite films or gels through rigid or soft stamps, respectively. Nevertheless, for rigid stamps used in hot embossing, (20−22) such as silicon chips patterned by electron-beam lithography or photolithography, there are concerns about the risk of damaging the costly and

fragile molds under such high pressure up to 100 bar. On the other hand, applying soft stamps such as the polydimethylsiloxane (PDMS) membrane (23,24) on the top of the perovskite gel with direct compression would easily lead to nanostripes, with the substrate exposed at some parts. Besides, the direct pattern on perovskites by electron-beam lithography (25) or laser beams (26) instead of utilizing the as-prepared stamps would give rise to unexpected adverse effects on the crystallization quality and homogeneity because of the poor tolerance of the perovskites to heat and high-energy particles. The other indirect approach is to deposit perovskite polycrystalline films on patterned substrates such as quartz glass, (27) silicon wafers, (28) and Si_3N_4, (29) or even biomaterials (30) by evaporation or spin-coating methods. However, the patterned substrates, which are fabricated with complicated and expensive processes, serve as the component of the device and thus are one-off, leading to high cost of perovskite-based devices and limitation of the substrates. Recently, periodical perovskite nanostripes based on the reusable and low-cost PDMS membrane by feasible phase transition with the assistance of methylamine (MA) gas and annealing treatment have been reported. (31) However, these kind of nanostripes can hardly serve as the integrated optical resonators due to high energy loss in the active layer in photovoltaic or light-emitting devices the as exposed-substrate part could lead to severe current leakage. (32−34) Moreover, the annealing treatment is not adaptable for some temperature-sensitive flexible substrates and electronic components. Consequently, realizing an integrated perovskite nanoresonator fabricated by a facile room-temperature solution process is still a challenge. Further developments on perovskite nanostripe-integrated waveguide structures with facile processing methods are of significance for extending the applications in optoelectronic devices.

Here, we demonstrate a solution-processed upside-down approach to fabricate photonic resonators with a certain range of controllable pattern geometry and waveguide thickness. We propose an approach of upside-down molding method by simply attaching desired nanopattern templates onto the flipped-over perovskite film to avoid possible template–substrate direct contact due to the weight of templates when the perovskite membranes are placed upward. This approach not only reveals the effect of the capillary force to make the gel penetrate into the nanoscale troughs of the template pattern but also can control the thickness of the waveguide layer because of the inversion of the perovskite membranes. Besides, we take full advantage of MA-induced phase transition and antisolvent-vapor-assisted method to optimize the crystal quality of our perovskite resonators. Finally, after simply optimizing the crystal quality and geometrical parameters of our perovskite resonators, we demonstrate that the patterned perovskites can achieve remarkable lasing emission with a threshold of 15.3 $\mu J/cm^2$ and line width of 0.52 nm at 782.9 nm. This work contributes an approach to realize controllable periodic perovskite nanostructures for emerging optoelectronic applications.

Results and Discussion

Controllable Periodic Nanostructures

Our upside-down molding method is suitable for general perovskite gels and precursors according to the mechanism. Here, considering the gels prepared by MA treatment exhibit excellent high-quality-film-forming ability, (35,36) we take the MA-induced gels as an example to show the whole process. The schematic procedures are shown in Figure 1 A soft PDMS stamp with the periodic pattern was covered on top of the as-prepared $MAPbI_3$ perovskite film (Figure 1a,b). Different from the conventional imprinting method in which the perovskite membranes are placed upward, we performed an upside-down process by reversing the substrate

and keeping the PDMS-covered area suspended in midair (Figure 1c). Then, we adopted a volatile amine gas, MA, to transform the raw perovskite film from the solid state to liquid-phase perovskite gel ($MAPbI_3 \cdot xCH_3NH_2$) at ultrafast speed (Figure 1d). (37) The proposed upside-down approach resorts to the capillary force to make the perovskite gel permeated into the narrow grooves of the soft stamp in dozens of seconds (Figure 1e). Besides, we can tune the thickness of the waveguide layer by changing the precursor concentration accordingly. This merit is unique to our method as no pressure is imposed. During the whole imprinting process, only a downward pulling force (stretching force) from the template's weight is exerted on the perovskite gel, which, however, is balanced by the physical adhesion force between the perovskite gel and the template. The amount of gel is well retained to form the waveguide layer with different thicknesses instead of being squeezed away by the external force (downward extrusion force) in the conventional imprint method. Typically, after removing the organic amine gases, the transparent gel would return to dark-brown solid perovskites at ultrafast speed without further treatment. However, when the soft stamp covers the perovskite gel, the release of the gases would be hindered and may lead to a transition in the crystal structure as the recrystallization process will be prolonged to around 1 h. The transparent perovskite gels attached by stamps turn light brown rather than pristine dark brown after such a long recrystallization time. The prolonged recrystallization will lead to worse surface morphology and decrease in photoluminescence (PL). More details would be discussed later in the sections below. Here, we propose to introduce dichloromethane (DCM) vapor treatment to accelerate the recrystallization under room temperature (Figure 1f).

DCM is a kind of volatile nonpolar solvent and often used as an antisolvent vapor for the growth of bulk perovskite crystals (38,39) and single-crystal membranes. (40) Here, liquid antisolvent

such as chlorobenzene cannot work due to the soft membrane blocking. Therefore, the volatile DCM was chosen to act as a gaseous antisolvent. After the perovskite gel permeated into the groove of the soft stamp, we introduced DCM vapor into the container, as shown in Figure S1. The PDMS-covered perovskite gels were rapidly saturated and crystallized along with the diffusion of gaseous DCM. The transparent perovskite gel then turned dark brown from the edge to the middle of the stamp along with the DCM vapor's diffusion. The recrystallization process would decrease from around 1 h (room-temperature volatilization) to 10–20 min. It is of great significance to optimize the fabrication process to be conducted in a mild environment for various application scenarios. Besides, the room-temperature solution-based fabrication approach would offer low energy consumption and low-cost processes. Finally, after removing the hydrophobic soft stamp (Figure 1g), a waveguide-integrated nanostructure without any exposed part was achieved for functioning optoelectronic devices such as the representative device of photonic resonators. Figure S2 shows the optical image of patterned and pristine perovskite films.

The upside-down method is the unique technique used to form continuous optical waveguide structures and various patterns simultaneously. As shown in Figure S3, we also imprinted the perovskite film using the conventional downward method (the membranes are placed upward during imprinting) as a comparison. For the formation of the waveguide layer, when the soft stamp is on top of the perovskite gel in the conventional downward imprint process, (23,24,31) the weight of the soft stamp or the extrinsic press through mechanical extrusion is the major contributor of imprinting patterns. However, these forces imposed on the liquid gel would easily lead to template–substrate direct contact, which is the main cause of the exposed substrate part, especially when the pristine film is thin. In contrast, the template-covered perovskite film is inverted in our method. The van der Waals force between the perovskite and

the template is the downward pulling force to the solution perovskite in the process. Such weak but sufficient pulling force allows the formation of the nanopattern and the waveguide layer simultaneously. As a result, the gap between the substrate and template can always be filled with perovskite gel and turn into the integrated waveguide structure after recrystallization. The comparison between the mode propagation profiles of the samples with (upside-down molding approach) and without (conventional approach) waveguiding layer are also detailed in Figure S4 and discussed in the Supporting Information Note 1. Regarding the pattern formation, the nano-to micron-sized grooves on the soft mold are sufficiently small. The liquid gel is propelled to enter the narrow spaces due to the capillary phenomenon, that is, the combined effect of surface tension and adhesive forces between the liquid and template.

Our approach applies to various photonic patterns in one- or two-dimensional structures. The morphologies of the pristine and patterned perovskite films are shown in Figure 2. The atomic force microscopy (AFM) image in Figure 2 shows the pristine perovskite film exhibiting a polycrystalline morphology with a roughness of 28.60 nm [root-mean-square (rms)]. In representative line scans along the direction of perovskite gratings (Figure 2b, horizontal solid line c,d), the rms roughness greatly decreases from 28.60 nm to merely 3.9 nm after the imprinting process. In most of the optoelectronic devices such as DFB laser, the ultrasmooth semiconductor surface can significantly reduce the lasing threshold, resulting from the minimal light scattering and loss in the waveguide. (22) Besides, the rms deviation of altitude across the grating peaks was only 1.75 nm (Figure 2b, vertical dashed line a,b). This indicates that the periodic change of the effective refractive index across the grating is extremely regular, and thus, the DFB structure can be precisely favored to a particular emission mode. Therefore, the DFB laser based on the regular geometric construction pattern with an ultrasmooth surface would

exhibit the properties of threshold and excellent monochromaticity. Figure 2c displays a two-dimensional dot-matrix perovskite pattern. This kind of pattern allows periodic modulation of the refractive index along two directions. (41) Overall, both patterns show excellent regularity that confirms that our method would be broadly applicable to different nanopatterns.

Organic amine gases not only can dissolve the solid perovskites such as other high-boiling-point polar solvents but also can reduce defects in the raw perovskite films through the reversible gas–solid interaction. (37)Figure 2d shows the scanning electron microscopy (SEM) image of the pristine film. The grain boundary is highly obvious. After the imprinting, a dense, smooth-surface perovskite grating emerged (Figure 2e). From the cross-sectional SEM images of the patterned perovskites (Figure 2f), we confirm that the liquid perovskite gel is always in close contact with the soft template when the substrate was inverted; no cracks or holes are observed from the cross-sectional image.

To understand the thickness of the waveguide on the effect of the nanopatterned structure, we fabricated a series of perovskite films with different precursor concentrations (1.0, 1.2, and 1.4 M). As can be seen from the cross-sectional SEM images (Figure S5), the teeth of the gratings almost have the same height, while the thickness of the waveguide layer increased with the precursor concentration. The waveguide thicknesses of the gratings made by 1.0 M (Figure S5a) and 1.2 M (Figure S5b) precursors are around 100 and 220 nm, respectively, while the waveguide thickness of 1.4 M counterparts is around 500 nm (Figure S5c). This is because the amount of liquid gel into the mold grooves is constant under given conditions; hence, the thicker pristine film results from the more perovskite gel between the substrate and the soft membrane.

To obtain a deeper understanding of the capillary phenomenon in groove formation, we conducted hydrophilic treatment on the soft molds. To be specific, the patterned soft molds were immersed in an aqueous solution of sodium dodecyl benzenesulfonate and then dried in an oven. The increase in surface energy is demonstrated in the smaller contact angle of water droplets on the treated PDMS molds when compared to the pristine membrane, as shown in Figure S6. The contact angle decreased from 121.5 to 114.2°, which implies the enhancement of the interaction between the molds and the gel after the treatment. The height profiles from the AFM of relevant perovskite gratings are shown in Figure 3a (made from pristine PDMS) and Figure 3b (made from treated PDMS). Interestingly, the groove depth increased from 80 to 100 nm after treatment. According to Young's equation (eq 1)

$$\gamma^{ls} = \gamma^{s} + \gamma^{l}\cos\theta \tag{1}$$

There are three kinds of interfacial energy on the three-phase intersection, including solid–vapor (γ^{s}), solid–liquid (γ^{ls}), and liquid–vapor (γ^{l}) interfacial energy, as shown in Figure 3c. The hydrophilic treatment increases the solid–vapor (γ^{s}) interfacial energy and may lead to better wettability. Therefore, the three-phase intersection would drop, and thus, we can achieve perovskite grating with increased grating height. Although the contact angle only decreased by 7.3° after hydrophilic treatment, the perovskite gel fills the entire grooves as the depth of the soft stamp is just around 100 nm.

Material Optimization

To better analyze the effect of this gas solvent-assisted imprinting process on the structure and quality of the perovskites, we conducted measurement on the PL spectrum and time-resolved PL (TRPL). Note that a planar soft stamp is used in the imprinting process here to eliminate the

effects from the grating structure onto the material crystal quality. Figure 3d shows that the PL intensities are significantly improved for the samples with amine treatment, no matter if it was covered with the soft stamp or not. Typically, the grain boundary and pin holes mean more defects/trap states in the perovskite membranes, which would lead to an increase in the nonradiative recombination and weak PL intensity. After the MA-induced solid–liquid conversion, the cured perovskite membranes show a smooth and dense morphology and the defects/trap states are effectively suppressed. Approximately 4-fold intensity enhancement can be observed from the MA-healed film and 2.5-fold improvement from the healed film covered by the PDMS membrane. It also shows that if amine gases were delayed when discharging from the perovskite gel because of soft membrane blocking, not only the surface morphology would become worse (31) but also lead to a decrease in PL intensity due to the pin holes, as shown in Figure S7. This is why we need DCM treatment to accelerate recrystallization. Unlike the SEM images with obvious pin holes as shown in Figure S7b, the DCM-induced perovskite patterns show smooth and dense surface morphology. Furthermore, the improvement in charge carrier properties was studied through the TRPL (Figure 3e). The carrier decay lifetimes of the pristine and imprinted perovskites are 5.47 ns (τ_1 = 4.35 ns, 81.74%; τ_2 = 10.47 ns, 18.26%) and 12.75 ns (τ_1 = 7.98 ns, 23.14%; τ_2 = 14.18 ns, 76.86%) respectively, from the biexponential fitting. The two components represent the defect states located at the surface and bulk, respectively. (39) The doubling in the lifetime from the imprinted film indicates the improvement of crystal quality through the stamping process. Additionally, the even prolonged lifetime of 17.49 ns (τ_1 = 10.55 ns, 46.30%; τ_2 = 23.48 ns, 53.70%) from the film just after MA post-treatment suggested the great reduction of traps and defects in the perovskite. Although the

delay of the release in MA during post-treatment in the imprinting process would affect the crystal quality, its film quality still shows apparent improvement compared to the pristine film.

We further studied the X-ray diffraction (XRD) patterns of the perovskite gratings that were recrystallized under different recrystallization conditions. Since the method of annealing the patterned perovskite gel has proven to be an alternative way for recrystallization, (31) we put the annealing recrystallization samples here as a comparison to confirm the gaseous DCM's ability to accelerate the recrystallization. As shown in Figure 3f, the peaks of the pristine perovskites located at 14.20 and 28.67° represent (110) and (220) planes, respectively. (42) For the patterned samples, the imprinting process alters the crystal orientation, where the dominating signals in XRD appear at 14.20 and 24.60°, corresponding to the (110) and (202) planes of the tetragonal perovskite structure of $MAPbI_3$. (42) Besides, using the annealing method to accelerate the recrystallization can contribute to much better crystal quality compared to room-temperature volatilization, as shown at around 10-fold higher intensity of characteristic peaks at 24.60° [(202) plane]. This claim is further attested by the significant narrowing of peak line widths from 0.2399° before treatment to 0.1216° after annealing. The antisolvent vapor-induced perovskite gratings also have characteristic peaks at 14.20 and 24.60°, which are the same as their annealing counterparts. Interestingly, the vapor-induced characteristic peak at 24.60° has about double intensity of the annealing-assisted samples, which implies that the antisolvent vapor-induced perovskite gratings have higher crystallinity in this lattice phase due to more efficient gas extraction.

Optical Properties

The light polarization absorption spectra of perovskite planar film and grating are shown in Figure S8. For the pristine film, the absorption curves of transverse electric (TE) polarized light (electric field parallel to gratings) coincide with transverse magnetic (TM) polarized light (electric field perpendicular to gratings). Differently, the absorption of TE polarized light in perovskite grating is slightly higher at the short-wavelength region when compared to the pristine planar film, while the TM polarized light remains unchanged. This shows the polarization-dependent absorption properties induced from the perovskite gratings with the nanoimprinted periodical nanostructures. According to the theory of effective medium approximation, (43,44) the extinction coefficients (imaginary part of the effective refractive index) of the TE-polarized and TM-polarized lights are separated in the grating structures. The absorption of light is, therefore, more desirable for TE polarization, resulting in a significant enhancement in TE-polarized light absorption, especially in the blue to green regions.

Furthermore, we studied the angle-resolved PL spectrum of the samples. There is a significant light emission enhancement at the angles of around ±7.5 and ±25° for the 320 nm gratings while no enhancement at any angles for the planar film, as shown in Figure 4a. The peak features originate from light coupling in the grating structures according to the grating equation. (45) Additionally, the overall enhancement of the PL intensity of grating is due to the combination of crystal quality improvement and optical resonance. The angle-independent emission curve from the pristine film conforms to the Lambertian radiation pattern as expected. To better analyze the angular distribution of the PL intensity, we conducted a full-wave simulation through the finite-difference time-domain (FDTD) method. The simulation results in Figure 4b show a similar angular distribution compared to experimental data. In the theoretical

results, the PL intensity of perovskite grating is weaker than that of the planar film at certain angles. However, from the experimental data, the perovskite grating always shows higher PL intensity than the film at all angles. This difference can be explained by the improved crystallinity of the perovskite, as discussed earlier. Moreover, the simulated angle-resolved PL spectrum of the pristine perovskite also coincides with the Lambertian radiation pattern (Figure 4c). Regarding the 320 nm period grating, four significant peaks exist in the radiation pattern (Figure 4d). The peaks were located at two emission angles of around ±7.5 and ±20° at the wavelength of around 780 nm. These simulation results are in good agreement with the experimental data. Combining with the PL emission results, our patterned perovskites show enhancement in both absorption and light-extraction efficiency, which is consistent with previous reports of enhanced performance for optoelectronics incorporated with photonic nanostructures. (1−5,37) The enhanced optical properties through our imprinting method could contribute to the optimization of performance in various optoelectronics, including solar cells, photodetectors, and light-emitting devices.

Perovskite Photonic Resonator-Based Lasers

Among the patterned semiconductors optoelectronics, DFB lasers require the dedicated design on the geometry parameters of the linear gratings. More importantly, the light scattering of guiding modes is highly sensitive to the surface roughness and homogeneity of the grating structure, which is the major cause of the deterioration of device lasing quality. Taking the advantage of excellently high gain from the perovskite material, (46) together with the improved crystal quality and uniform gratings from our stamping method, it is possible to realize the highly controllable DFB laser after parameter optimizations.

In demonstrating the lasing phenomenon from perovskite DFB laser, the grating parameters are designed through the Bragg eq 2 $\lambda_L = \frac{2n_{eff}\Lambda}{m}$ (2)where λ_L, n_{eff}, Λ, and m are the resonant wavelength, effective refractive index, grating periodicity, and order of mode, respectively. In the following discussion, the DFB lasers with second-order mode (m = 2) are designed because of their close-to-normal out-coupling from the grating structure, also for the ease of fabrication. This is beneficial to both device quality and allows easier lasing characterizations.

We fabricated and examined the lasing characteristics of one-dimensional perovskite gratings with a periodicity (Λ) of 320 nm, whose resonance wavelength roughly matches with the PL emission range of the perovskite materials. The details of lasing characterization are described in Materials and Methods. As shown in Figure 5a,b, strong lasing at the wavelength of 782.9 nm is observed from our perovskite grating under the reasonable threshold of 15.3 μJ/cm^2. The effective refractive index of the laser mode of n_{eff} = 2.446 is obtained according to the Bragg equation. This value is also close to the simulated fundamental TM mode effective index (n_{eff} = 2.388) from the 320 nm perovskite waveguide using the finite-different eigenmode method. It shows that the feedback from the grating structure has amplified the fundamental TM mode and allows it to lase in our device. Additionally, the emission linewidth, as displayed in Figure 5c, is significantly reduced from around 40 nm down to less than 5 nm, which demonstrates the property of emission narrowing in the laser oscillation. It shall be noted that the linewidths of the laser peaks as shown in Figure 5a,c were limited by the system resolution of the spectrometer (~5 nm). The higher-resolution grating (1200 lpmm) was used to resolve the lasing peak. The linewidth of $\Delta\lambda$ = 0.52 nm at the fluence of just above the threshold was obtained; see Figure 5d. The high Q-factor of over 1500 indicates the excellent cavity qualities from the sample fabricated using the upside-down molding method.

Although the lasing linewidth we demonstrated here is relatively larger than some other photonic crystal perovskite DFB lasers, (22,47) it is the limitations that come from the large pumping area (5 mm × 0.3 mm). With the longer stripe excitation, stronger feedback can be provided from more periods of DFB gratings. Hence, the threshold can be greatly reduced with large-area excitation. However, obtaining lasing from a large area easily suffers from the inhomogeneity of the sample, especially in our spin-coated solution-based devices. The little unevenness of the layer thickness and periodicity usually can result in the broadening of laser linewidth, together with the slight increase in the lasing threshold. Undoubtedly, it is possible to narrow the emission linewidth by using microscopic excitations on only a few tens of the micron-sized region (see Figure S9, where laser linewidth of 0.38 nm was achieved). However, the threshold and linewidth demonstrated here have already been comparable to the previously reported perovskite DFB lasers; see the comparison table in Table S1. This demonstrates the possibilities of making high-quality laser devices over a large imprinted area using this approach.

Additionally, the emission dependence on the excitation stripe orientation is also tested and illustrated in Figure 5d. The lasing phenomenon can only be observed when the pumping stripe is in the perpendicular orientation with respect to the grating lines, while only weak PL is emitted in the case of parallel orientation. This result further attested that the feedback from DFB structures is the major contribution to the lasing emission from our perovskite devices. It shows that with our new molding method, it is possible to engineer large-area devices with controllable periodic nanostructures for a variety of use. The second-order laser emission that we demonstrate here shows the head-on direction of the grating, which also promotes the potential of applying into the surface-emitting laser at the near-infrared region for different applications.

Conclusions

In summary, we have demonstrated an upside-down molding approach to fabricate perovskite photonic resonators with a certain range of controllable geometry and waveguide layer. We demonstrate that the alteration of the templates' surface tension could change the depth of the patterns. Meanwhile, the photonic structure with different waveguide layer thicknesses can be well achieved through the adjustment of the pristine membrane thickness. Besides, we reveal that the permeation of MA-induced perovskite gel into the narrow grooves of the mold is driven by the capillary force under inversion circumstances. We further optimized the membranes' morphology by simply using the volatile DCM vapor treatment to accelerate the crystallization during imprinting.

After imprinting and morphology optimization, the perovskites with high-quality resonators integrated with an optical waveguide layer were achieved. We identify the enhancement in the absorption and emission properties from the patterned perovskite film. Finally, we utilize the imprinted linear grating structure as a demonstration and obtained a remarkable threshold of 15.3 $\mu J/cm^2$ and linewidth of around 0.52 nm under pulsed excitations. Our work provides a strategy to fabricate geometrical parameter-controllable perovskite photonic resonators at room temperature. It suggests the promising applications of solution-based perovskites on different substrates including rigid and flexible ones. We believe that this new approach can inspire the industry in commercializing high-quality perovskite-based devices, such as solar cells, LEDs, and lasers.

Materials and Methods

Materials

Lead iodide (PbI_2, 99.99%) and MA iodide (MAI) were purchased from TCl and Dyesol, separately. MA chloride (99.5%, MACl) was purchased from Xi'an Polymer Light Technology Corp. Dimethylformamide (DMF, 99%), dimethyl sulfoxide (DMSO, 99%), and chlorobenzene were (CB, 99.80%) bought from Acros Organics. MA (33 wt % in absolute ethanol) was purchased from Aldrich. Sodium dodecyl benzenesulfonate was purchased from J&K Chemical. SYLGARD 184 silicone elastomer kit including the base and curing agent was brought from Dow Corning. All the chemicals and solutions were used as received without further purification.

Pristine Perovskite Fabrication

Glass substrates were consecutively cleaned by ultrasonic treatment using detergent, deionized (DI) water, acetone, and ethanol and then dried in the oven. The substrates were exposed under ultraviolet ozone (UVO) for 20 min before use. For the perovskite precursor, stoichiometric PbI_2, MAI, and MACl (molar ratio = 1:1:0.15) were dissolved in 1 mL of the DMF and DMSO mixture (volume ratio 4:1). The precursors were stirred at room temperature for 2 h and then filtered by 0.22 μm PTFE syringe filters. The perovskite precursor was spin-coated onto the substrate at 5000 rpm for 20 s, and 500 μL of CB was added dropwise to it at 15 s with uniform velocity. After the spin coating process, the substrate was annealed at 100 °C for 10 min. Spin coating and annealing were carried out in a nitrogen glovebox. Note that other room temperature-fabricated pristine films can also be appropriate for the following imprinting procedure. (48)

Nanostructure Fabrication

The soft PDMS stamps were prepared by adding SYLGARD 184 silicone elastomer base and curing agent (v/v = 10:1) on the patterned or flat silicon wafer. After the elimination of the bubbles in the mixture in the vacuum state for 20 min, the covered silicon wafer was annealed at 65 °C overnight to form the solid-state PDMS molds. The PDMS mold was stuck on a pristine perovskite thin film, and then, the substrate was inverted and placed in a Petri dish. The Petri dish was filled with gaseous MA drop by drop into 20 μL of MA solution of ethanol. The uncovered perovskites turned transparent immediately, while the PDMS-covered part completed this transition, taking several minutes. After all the brown perovskites turn to transparent perovskite gel, dozens of seconds were necessary for the liquid perovskite gel to permeate into the narrow slit of the soft molds. The recrystallization of the perovskite gel was performed using either room-temperature volatilization, 120 °C annealing, or DCM vapor treatment. The DCM vapor treatment means transferring the patterned perovskite gel into another Petri dish filled with gaseous DCM for 10–20 min. After finishing the recrystallization, the PDMS mold was torn away, leading to the formation of imprinted perovskites. All the processes completed in the nitrogen glovebox. For the hydrophilic treatment on the patterned soft molds, we dissolved 1 mol sodium dodecyl benzenesulfonate in 40 mL of DI water and then immersed the molds in the aqueous solution for 10 min. Finally, the molds were transferred to an oven and dried at 100 °C for 6 h before use.

Characterization of Materials

The morphology of the pristine and patterned perovskites was characterized by SEM (Hitachi S-4800 FEG) and AFM (NT-MDT NTEGRA Prima). The XRD spectrum was achieved using a

Bruker D2 Phaser, which was collected in the angular range of 5–50° (2θ) with a step size of 0.02. The optical absorption spectrum and angle-resolved PL spectrum were collected by an angle-resolved spectrum system (R1, Ideaoptics, China) equipped with a highly sensitive spectrometer (NOVA, Ideaoptics, China). Polarized light was achieved after placing a polarizing prism between the light source and the sample.

Characterization of Laser Devices

The perovskite DFB samples were optically pumped by a Ti-Sapphire regenerative amplifier-seeded optical parametric amplifier system with a wavelength of 610 nm, a repetition rate of 1 kHz, and a pulse width of 100 fs. The excitation spot was elongated through a cylindrical lens and then focused down to a laser stripe with an area of 5 mm × 0.3 mm on the sample. The laser emission from the perovskite sample was filtered by a dichroic beam splitter (632.8 nm 45° RazorEdge Dichroic, Semrock), collected by a fiber-coupled Acton SpectraPro 500i spectrometer (150 and 1200 lpmm gratings), and the spectra were measured by a detector (Newton EMCCD Camera, Andor, Oxford Instruments).

ASSOCIATED CONTENT

Supporting Information

The Supporting Information is available free of charge.

Photographic images, SEM images of grating, FDTD simulations, contact angles and AFM images, absorption spectrum, and lasing spectrum

Author Contributions

L.N. and W.K.N. contributed equally to this work. L.N. accomplished most of the experimental works and composed most the part of the manuscript. W.K.N. finished the laser emission relevant characterization and wrote the optical part. Z.L. conceived the original idea, and X.R. conducted the optical simulation. T.Y. and C.W.L. provided imprinting templates. G.M. drew some schematic diagrams for the manuscript. K.S.W. and W.C.H.C. guided the manuscript writing.

Notes

The authors declare no competing financial interest.

ACKNOWLEDGMENTS

This research was supported by the Equipment Fund and the Seed Fund (grant nos. 2019157209 and 201811159147) from the University Grant Council of the University of Hong Kong and the General Research Fund (Grant nos. 17204117, 17200518 17201819, and 17211220) and Collaboration Research Fund (C7035-20G) from Hong Kong Special Administrative Region, China. W.K.N. and K.S.W. acknowledge the financial support of the Research Grants Council of Hong Kong (grant no. AoE/P02/12) and William Mong Institute of Nano Science and Technology (grant no. WMINST19/SC04). T.B.Y. thanks the National Natural Science Foundation of China (no. 51703092) for financial support. X.G.R. would like to acknowledge the financial support of the National Natural Science Foundation of China under grant 61701003. The authors acknowledge the assistance of SUSTech Core Research Facilities and Dr. Wang Yao for the fabrication of silicon grating stamps. We acknowledge Dr. Haiwei Yin and Shanghai

Ideaoptics Corp. Ltd. for the support on the angle-resolved spectrum measurements and Taili Liu from the City University of Hong Kong, China, for their help in XRD characterizations.

Graphical abstract

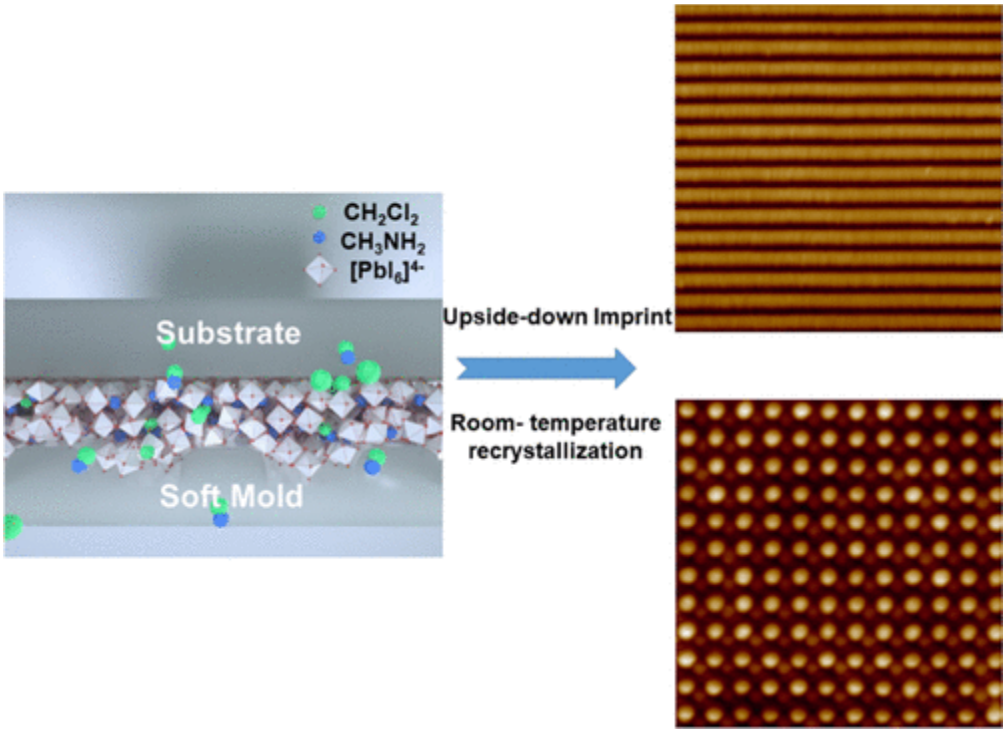

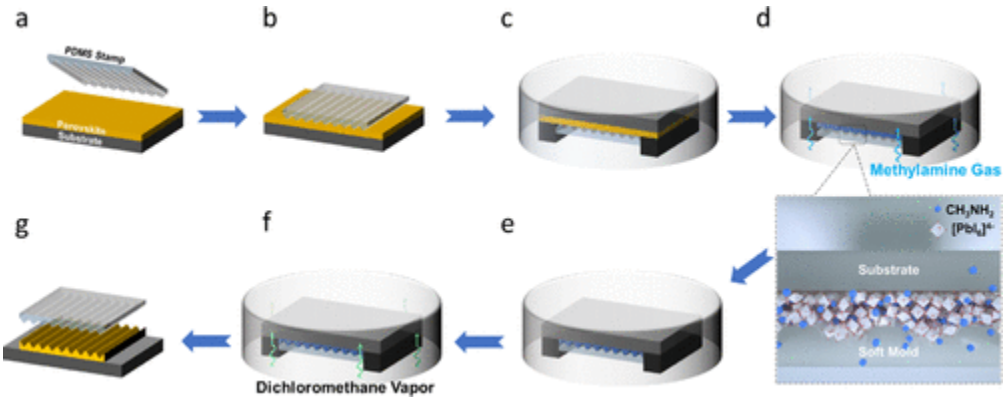

Figure 1. Schematic illustration of the upside-down nanoimprinting approach for the fabrication of perovskite periodic nanostructures: (a) as-prepared $MAPbI_3$ film; (b) cover the soft template on the top of perovskite film; (c) invert the sample in the container; (d) introduce MA in the container; (e) MA permeate into the molds; (f) DCM vapor treatment to eliminate excess MA; (g) remove the soft template.

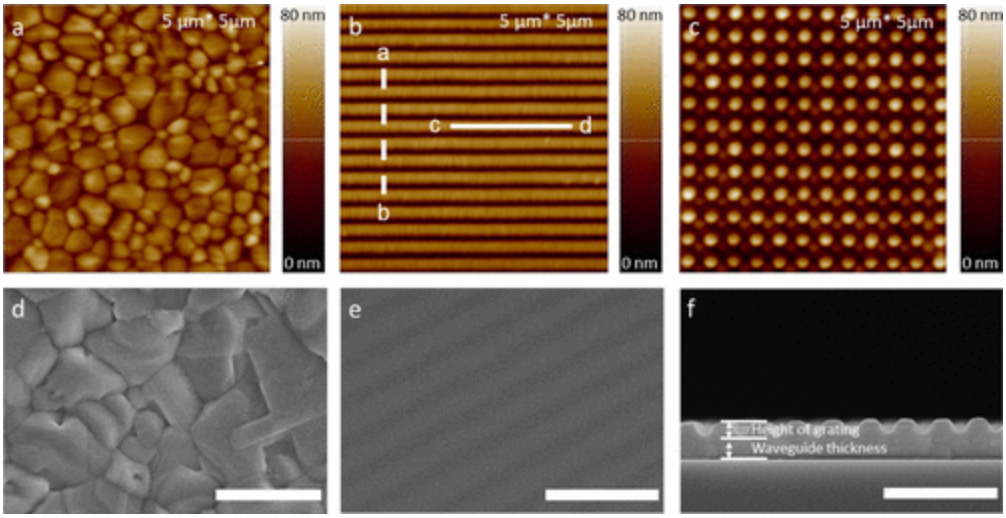

Figure 2. Atomic force micrograph of (a) pristine perovskite film; (b) one-dimensional linear perovskite grating (320 nm in period); and (c) two-dimensional photonic perovskite pattern. The SEM images of (d) top-view pristine perovskite film; (e) top view and (f) cross section of perovskite grating with the periodicity of 320 nm. The inset scale bar represents 1 μm.

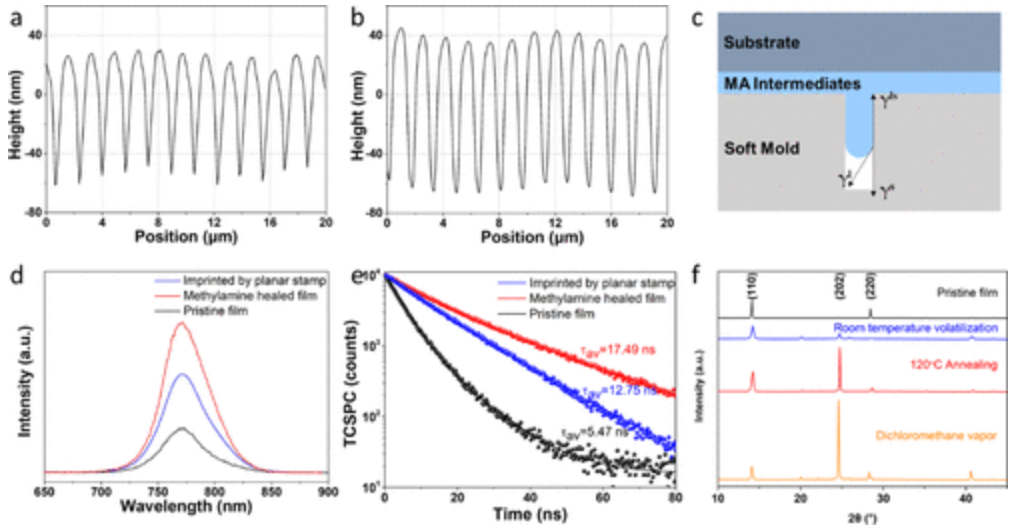

Figure 3. Height profiles of perovskite gratings: imprinting by (a) pristine PDMS molds; (b) PDMS molds with hydrophilic treatment; (c) schematic illustration of capillary force during the imprinting; (d) PL spectrum and (e) time-resolved PL of the perovskites; (f) XRD spectrum of pristine and patterned perovskites through different recrystallization methods.

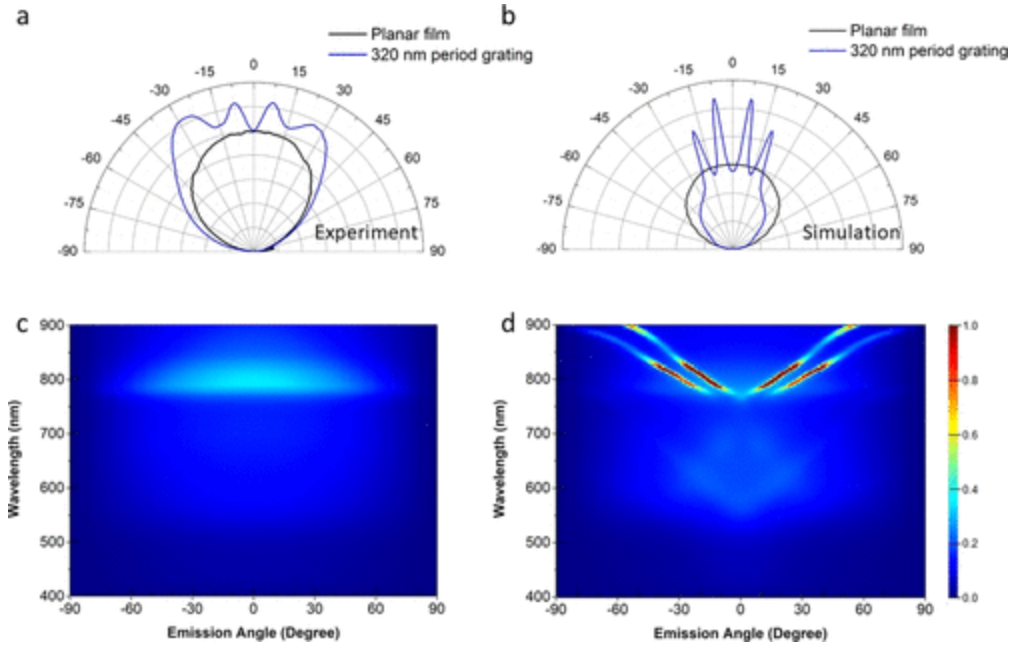

Figure 4. Angle-resolved PL spectra of perovskites through (a) experiment; (b) simulation. Angular- and wavelength-dependent radiation power of (c) planar perovskite film; (d) 320 nm in period perovskite grating.

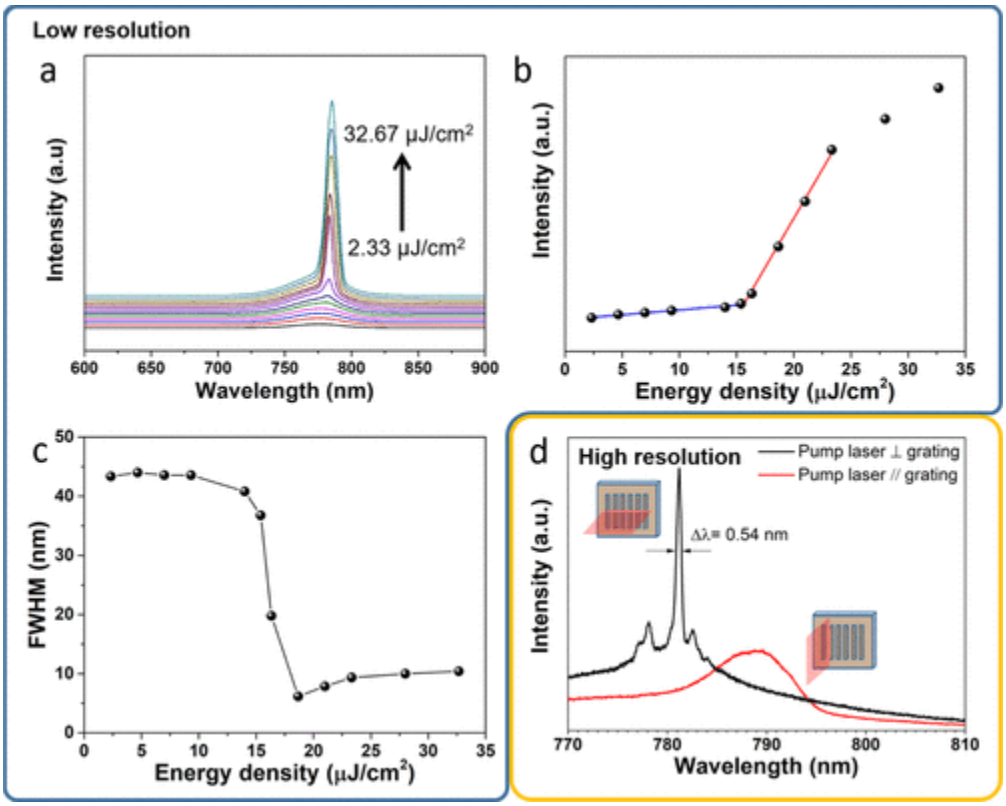

Figure 5. Emission spectra of DCM vapor-induced 320 nm period gratings: (a) evolution of the emission spectrum with pump laser under λ_p = 610 nm excitation; (b) laser output power as a function of pump laser intensity; (c) evolution of the emission full width at half-maximum from the 320 nm period perovskite grating; (d) laser emission spectrum measured at different excitation orientations. A low-resolution spectrometer grating was used in subfigures (a–c), and a high-resolution grating in subfigure (d).

REFERENCES

(1) Bermel, P.; Luo, C.; Zeng, L.; Kimerling, L. C.; Joannopoulos, J. D. Improving Thin-Film Crystalline Silicon Solar Cell Efficiencies with Photonic Crystals. Opt. Express 2007, 15, 16986.

(2) Zhou, D.; Biswas, R. Photonic Crystal Enhanced Light-Trapping in Thin Film Solar Cells. J. Appl. Phys. 2008, 103, 093102.

(3) Yang, J.-K.; Seo, M.-K.; Hwang, I.-K.; Kim, S.-B.; Lee, Y.-H. Polarization-Selective Resonant Photonic Crystal Photodetector. Appl. Phys. Lett. 2008, 93, 211103.

(4) Zhou, W.; Min, G.; Song, Z.; Zhang, J.; Liu, Y.; Zhang, J. Enhanced Efficiency of Light Emitting Diodes with a Nano-Patterned Gallium Nitride Surface Realized by Soft UV Nanoimprint Lithography. Nanotechnology 2010, 21, 205304.

(5) Kim, S. H.; Lee, K.-D.; Kim, J.-Y.; Kwon, M.-K.; Park, S.-J. Fabrication of Photonic Crystal Structures on Light Emitting Diodes by Nanoimprint Lithography. Nanotechnology 2007, 18, 055306.

(6) Shindo, T.; Okumura, T.; Ito, H.; Koguchi, T.; Takahashi, D.; Atsumi, Y.; Kang, J.; Osabe, R.; Amemiya, T.; Nishiyama, N.; Arai, S. GaInAsP/InP Lateral-Current-Injection Distributed Feedback Laser with a-Si Surface Grating. Opt. Express 2011, 19, 1884.

(7) Morthier, G.; Abbasi, A.; Verbist, J.; Keyvaninia, S.; Yin, X.; Lelarge, F.; Duan, G. H.; Bauwelinck, J.; Roelkens, G. High-Speed Directly Modulated Heterogeneously Integrated InP/Si DFB Laser. European Conference on Optical Communication; ECOC, 2016.

(8) Matsuo, S.; Fujii, T.; Hasebe, K.; Takeda, K.; Sato, T.; Kakitsuka, T. Directly Modulated Buried Heterostructure DFB Laser on SiO_2/ Si Substrate Fabricated by Regrowth of InP Using Bonded Active Layer. Opt. Express 2014, 22, 12139.

(9) Lan, H.; Ding, Y. Nanoimprint Lithography. In Lithography; Wang, M., Ed.; InTech, 2010; pp 458−488.

(10) Chou, S. Y.; Krauss, P. R.; Renstrom, P. J. Imprint Lithography with 25-Nanometer Resolution. Science 1996, 272, 85−87.

(11) Lin, K.; Xing, J.; Quan, L. N.; de Arquer, F. P. G.; Gong, X.; Lu, J.; Xie, L.; Zhao, W.; Zhang, D.; Yan, C.; Li, W.; Liu, X.; Lu, Y.; Kirman, J.; Sargent, E. H.; Xiong, Q.; Wei, Z. Perovskite LightEmitting Diodes with External Quantum Efficiency Exceeding 20 per Cent. Nature 2018, 562, 245−248.

(12) Huang, H.; Raith, J.; Kershaw, S. V.; Kalytchuk, S.; Tomanec, O.; Jing, L.; Susha, A. S.; Zboril, R.; Rogach, A. L. Growth Mechanism of Strongly Emitting CH3NH3PbBr3 Perovskite Nanocrystals with a Tunable Bandgap. Nat. Commun. 2017, 8, 996.

(13) Pan, W.; Wu, H.; Luo, J.; Deng, Z.; Ge, C.; Chen, C.; Jiang, X.; Yin, W.; Niu, G.; Zhu, L.; Yin, L.; Zhou, Y.; Xie, Q.; Ke, X. Cs2AgBiBr6 Single-Crystal X-Ray Detectors with a Low Detection Limit. Nat. Photonics 2017, 11, 726.

(14) Ye, F.; Lin, H.; Wu, H.; Zhu, L.; Huang, Z.; Ouyang, D.; Niu, G.; Choy, W. C. H. High-Quality Cuboid CH3NH3PbI3 Single Crystals for High Performance X-Ray and Photon Detectors. Adv. Funct. Mater. 2019, 29, 1806984.

(15) Jeon, N. J.; Noh, J. H.; Kim, Y. C.; Yang, W. S.; Ryu, S.; Seok, S. I. Il. Solvent Engineering for High-Performance Inorganic-Organic Hybrid Perovskite Solar Cells. Nat. Mater. 2014, 13, 897−903.

(16) Zhang, Q.; Ha, S. T.; Liu, X.; Sum, T. C.; Xiong, Q. RoomTemperature near-Infrared High-Q Perovskite Whispering-Gallery Planar Nanolasers. Nano Lett. 2014, 14, 5995.

(17) Xu, W.; Hu, Q.; Bai, S.; Bao, C.; Miao, Y.; Yuan, Z.; Borzda, T.; Barker, A. J.; Tyukalova, E.; Hu, Z.; Kawecki, M.; Wang, H.; Yan, Z.; Liu, X.; Shi, X.; Uvdal, K.; Fahlman, M.; Zhang, W.; Duchamp, M.; Liu, J.-M.; Petrozza, A.; Wang, J.; Liu, L.-M.; Huang, W.; Gao, F. Rational Molecular Passivation for High-Performance Perovskite Light-Emitting Diodes. Nat. Photonics 2019, 13, 418−424.

(18) Wang, L.; Zhou, H.; Hu, J.; Huang, B.; Sun, M.; Dong, B.; Zheng, G.; Huang, Y.; Chen, Y.; Li, L.; Xu, Z.; Li, N.; Liu, Z.; Chen, Q.; Sun, L.-D.; Yan, C.-H. A Eu 3+-Eu 2+ Ion Redox Shuttle Imparts Operational Durability to Pb-I Perovskite Solar Cells. Science 2019, 363, 265−270.

(19) Yakunin, S.; Sytnyk, M.; Kriegner, D.; Shrestha, S.; Richter, M.; Matt, G. J.; Azimi, H.; Brabec, C. J.; Stangl, J.; Kovalenko, M. V.; Heiss, W. Detection of X-Ray Photons by Solution-Processed Lead Halide Perovskites. Nat. Photonics 2015, 9, 444−449.

(20) Pourdavoud, N.; Haeger, T.; Mayer, A.; Cegielski, P. J.; Giesecke, A. L.; Heiderhoff, R.; Olthof, S.; Zaefferer, S.; Shutsko, I.; Henkel, A.; Becker-Koch, D.; Stein, M.; Cehovski, M.; Charfi, O.; Johannes, H. H.; Rogalla, D.; Lemme, M. C.; Koch, M.; Vaynzof, Y.; Meerholz, K.; Kowalsky, W.; Scheer, H. C.; Görrn, P.; Riedl, T. Room-Temperature Stimulated Emission and Lasing in Recrystallized Cesium Lead Bromide Perovskite Thin Films. Adv. Mater. 2019, 31, 1903717.

(21) Pourdavoud, N.; Mayer, A.; Buchmüller, M.; Brinkmann, K.; Häger, T.; Hu, T.; Heiderhoff, R.; Shutsko, I.; Görrn, P.; Chen, Y.; Scheer, H. C.; Riedl, T. Distributed Feedback Lasers Based on MAPbBr3. Adv. Mater. Technol. 2018, 3, 1700253.

(22) Pourdavoud, N.; Wang, S.; Mayer, A.; Hu, T.; Chen, Y.; Marianovich, A.; Kowalsky, W.; Heiderhoff, R.; Scheer, H.-C.; Riedl, T. Photonic Nanostructures Patterned by Thermal Nanoimprint Directly into Organo-Metal Halide Perovskites. Adv. Mater. 2017, 29, 1605003.

(23) Jeong, B.; Hwang, I.; Cho, S. H.; Kim, E. H.; Cha, S.; Lee, J.; Kang, H. S.; Cho, S. M.; Choi, H.; Park, C. Solvent-Assisted Gel Printing for Micropatterning Thin Organic-Inorganic Hybrid Perovskite Films. ACS Nano 2016, 10, 9026−9035.

(24) Jeong, B.; Han, H.; Kim, H. H.; Choi, W. K.; Park, Y. J.; Park, C. Polymer-Assisted Nanoimprinting for Environment- and PhaseStable Perovskite Nanopatterns. ACS Nano 2020, 14, 1645−1655.

(25) Xiao, C.; Li, Z.; Guthrey, H.; Moseley, J.; Yang, Y.; Wozny, S.; Moutinho, H.; To, B.; Berry, J. J.; Gorman, B.; Yan, Y.; Zhu, K.; AlJassim, M. Mechanisms of Electron-Beam-Induced Damage in Perovskite Thin Films Revealed by Cathodoluminescence Spectroscopy. J. Phys. Chem. C 2015, 119, 26904−26911.

(26) Zhizhchenko, A.; Syubaev, S.; Berestennikov, A.; Yulin, A. V.; Porfirev, A.; Pushkarev, A.; Shishkin, I.; Golokhvast, K.; Bogdanov, A. A.; Zakhidov, A. A.; Kuchmizhak, A. A.; Kivshar, Y.

S.; Makarov, S. V. Single-Mode Lasing from Imprinted Halide-Perovskite Microdisks. ACS Nano 2019, 13, 4140−4147.

(27) Chen, S.; Roh, K.; Lee, J.; Chong, W. K.; Lu, Y.; Mathews, N.; Sum, T. C.; Nurmikko, A. A Photonic Crystal Laser from Solution Based Organo-Lead Iodide Perovskite Thin Films. ACS Nano 2016, 10, 3959−3967.

(28) Saliba, M.; Wood, S. M.; Patel, J. B.; Nayak, P. K.; Huang, J.; Alexander-Webber, J. A.; Wenger, B.; Stranks, S. D.; Hörantner, M. T.; Wang, J. T.-W.; Nicholas, R. J.; Herz, L. M.; Johnston, M. B.; Morris, S. M.; Snaith, H. J.; Riede, M. K. Structured OrganicInorganic Perovskite toward a Distributed Feedback Laser. Adv. Mater. 2016, 28, 923−929.

(29) Cha, H.; Bae, S.; Lee, M.; Jeon, H. Two-Dimensional Photonic Crystal Bandedge Laser with Hybrid Perovskite Thin Film for Optical Gain. Appl. Phys. Lett. 2016, 108, 181104.

(30) Xing, G.; Kumar, M. H.; Chong, W. K.; Liu, X.; Cai, Y.; Ding, H.; Asta, M.; Grätzel, M.; Mhaisalkar, S.; Mathews, N.; Sum, T. C. Solution-Processed Tin-Based Perovskite for Near-Infrared Lasing. Adv. Mater. 2016, 28, 8191.

(31) Mao, J.; Sha, W. E. I.; Zhang, H.; Ren, X.; Zhuang, J.; Roy, V. A. L.; Wong, K. S.; Choy, W. C. H. Novel Direct Nanopatterning Approach to Fabricate Periodically Nanostructured Perovskite for Optoelectronic Applications. Adv. Funct. Mater. 2017, 27, 1606525.

(32) Wong, A. B.; Lai, M.; Eaton, S. W.; Yu, Y.; Lin, E.; Dou, L.; Fu, A.; Yang, P. Growth and Anion Exchange Conversion of CH3NH3PbX3 Nanorod Arrays for Light-Emitting Diodes. Nano Lett. 2015, 15, 5519.

(33) Li, G.; Rivarola, F. W. R.; Davis, N. J. L. K.; Bai, S.; Jellicoe, T. C.; De La Peña, F.; Hou, S.; Ducati, C.; Gao, F.; Friend, R. H.; Greenham, N. C.; Tan, Z. K. Highly Efficient Perovskite Nanocrystal Light-Emitting Diodes Enabled by a Universal Crosslinking Method. Adv. Mater. 2016, 28, 3528.

(34) Li, G.; Tan, Z. K.; Di, D.; Lai, M. L.; Jiang, L.; Lim, J. H. W.; Friend, R. H.; Greenham, N. C. Efficient Light-Emitting Diodes Based on Nanocrystalline Perovskite in a Dielectric Polymer Matrix. Nano Lett. 2015, 15, 2640.

(35) Ye, F.; Wu, H.; Qin, M.; Yang, S.; Niu, G.; Lu, X.; Wang, J.; Mitzi, D. B.; Choy, W. C. H. High-Quality MAPbBr3 Cuboid Film with Promising Optoelectronic Properties Prepared by a Hot Methylamine Precursor Approach. ACS Appl. Mater. Interfaces 2020, 12, 24498.

(36) Noel, N. K.; Habisreutinger, S. N.; Wenger, B.; Klug, M. T.; Hörantner, M. T.; Johnston, M. B.; Nicholas, R. J.; Moore, D. T.; Snaith, H. J. A Low Viscosity, Low Boiling Point, Clean Solvent System for the Rapid Crystallisation of Highly Specular Perovskite Films. Energy Environ. Sci. 2017, 10, 145.

(37) Zhou, Z.; Wang, Z.; Zhou, Y.; Pang, S.; Wang, D.; Xu, H.; Liu, Z.; Padture, N. P.; Cui, G. Methylamine-Gas-Induced Defect-Healing Behavior of CH 3 NH 3 PbI 3 Thin Films for Perovskite Solar Cells. Angew. Chem. Int. Ed. 2015, 54, 9705−9709.

(38) Saidaminov, M. I.; Adinolfi, V.; Comin, R.; Abdelhady, A. L.; Peng, W.; Dursun, I.; Yuan, M.; Hoogland, S.; Sargent, E. H.; Bakr, O. M. Planar-Integrated Single-Crystalline Perovskite Photodetectors. Nat. Commun. 2015, 6, 8724.

(39) Shi, D.; Adinolfi, V.; Comin, R.; Yuan, M.; Alarousu, E.; Buin, A.; Chen, Y.; Hoogland, S.; Rothenberger, A.; Katsiev, K.; Losovyj, Y.; Zhang, X.; Dowben, P. A.; Mohammed, O. F.; Sargent, E. H.; Bakr, O. M. Low Trap-State Density and Long Carrier Diffusion in Organolead Trihalide Perovskite Single Crystals. Science 2015, 347, 519−522.

(40) Lédée, F.; Trippé-Allard, G.; Diab, H.; Audebert, P.; Garrot, D.; Lauret, J.-S.; Deleporte, E. Fast Growth of Monocrystalline Thin Films of 2D Layered Hybrid Perovskite. CrystEngComm 2017, 19, 2598−2602.

(41) Lodahl, P. All-Solid-State Quantum Optics Employing Quantum Dots in Photonic Crystals. In Woodhead Publishing Series in Electronic and Optical Materials; Jahnke, F., Ed.; Woodhead Publishing, 2012; pp 395−422e.

(42) Oku, T. Crystal Structures of CH3NH3PbI3 and Related Perovskite Compounds Used for Solar Cells. Solar Cells-New Approaches and Reviews; InTech, 2015; Vol. 1.

(43) Brundrett, D. L.; Glytsis, E. N.; Gaylord, T. K. Homogeneous Layer Models for High-Spatial-Frequency Dielectric Surface-Relief Gratings: Conical Diffraction and Antireflection Designs. Appl. Opt. 1994, 33, 2695.

(44) Zhiwen, W.; Jinliang, G.; Aimei, D.; Bo, C. Mechanism Analyzation of the Effects of Grating Parameters on Polarization Transmission of Single-Layer Nanowire Gratings. Proc. Inst. Mech. Eng.-Part N J. Nanoeng. Nanosyst. 2018, 232, 41−47.

(45) Ziebarth, J. M.; Saafir, A. K.; Fan, S.; McGehee, M. D. Extracting Light from Polymer Light-Emitting Diodes Using Stamped Bragg Gratings. Adv. Funct. Mater. 2004, 14, 451−456.

(46) Xing, G.; Mathews, N.; Lim, S. S.; Yantara, N.; Liu, X.; Sabba, D.; Grätzel, M.; Mhaisalkar, S.; Sum, T. C. Low-Temperature Solution-Processed Wavelength-Tunable Perovskites for Lasing. Nat. Mater. 2014, 13, 476.

(47) Schünemann, S.; Brittman, S.; Chen, K.; Garnett, E. C.; Tüysüz, H. Halide Perovskite 3D Photonic Crystals for Distributed Feedback Lasers. ACS Photonics 2017, 4, 2522−2528.

(48) Zhang, H.; Cheng, J.; Li, D.; Lin, F.; Mao, J.; Liang, C.; Jen, A. K.-Y.; Grätzel, M.; Choy, W. C. H. Toward All Room-Temperature, Solution-Processed, High-Performance Planar Perovskite Solar Cells: A New Scheme of Pyridine-Promoted Perovskite Formation. Adv. Mater. 2017, 29, 1604695.